NASA Technical Paper 3369

September 1993

Effects of Internal Yaw-Vectoring Devices on the Static Performance of a Pitch-Vectoring Nonaxisymmetric Convergent-Divergent Nozzle

Scott C. Asbury

NASA Technical Paper 3369

1993

Effects of Internal Yaw-Vectoring Devices on the Static Performance of a Pitch-Vectoring Nonaxisymmetric Convergent-Divergent Nozzle

Scott C. Asbury

Langley Research Center

Hampton, Virginia

Abstract

An investigation was conducted in the static test facility of the Langley 16-Foot Transonic Tunnel to evaluate the internal performance of a nonaxisymmetric convergent-divergent nozzle designed to have simultaneous pitch and yaw thrust-vectoring capability. This concept utilized divergent flap deflection for thrust vectoring in the pitch plane and flow-turning deflectors installed within the divergent flaps for yaw thrust vectoring. Modifications consisting of reducing the sidewall length and deflecting the sidewall outboard were investigated as means to increase yaw-vectoring performance. This investigation studied the effects of multiaxis (pitch and yaw) thrust vectoring on nozzle internal performance characteristics. All tests were conducted with no external flow, and nozzle pressure ratio was varied from 2.0 to approximately 13.0.

The results indicate that this nozzle concept can successfully generate multiaxis thrust vectoring. Deflection of the divergent flaps produced resultant pitch vector angles that, although dependent on nozzle pressure ratio, were nearly equal to the geometric pitch vector angle. Losses in resultant thrust due to pitch vectoring were small or negligible. The yaw deflectors produced resultant yaw vector angles up to 21° that were controllable by varying yaw deflector rotation. However, yaw deflector rotation resulted in significant losses in thrust ratios and, in some cases, nozzle discharge coefficient. Either of the sidewall modifications generally reduced these losses and increased maximum resultant yaw vector angle. During multiaxis (simultaneous pitch and yaw) thrust vectoring, little or no cross coupling between the thrust-vectoring processes was observed.

Introduction

Mission requirements for the next generation multirole fighter may necessitate aircraft capable of operating over a broader range of flight conditions than previously thought possible. Typical mission scenarios in the future may require aircraft to operate from short fields or bomb-damaged runways, to cruise supersonically, and to have increased levels of maneuverability at transonic and supersonic speeds. To survive air combat engagements, aircraft will require improved handling qualities at high angles of attack, including brief excursions into the poststall region. Several investigations have shown that significant advantages are gained in air combat with the ability to perform transient maneuvers at low speeds and high angles of attack. (See refs. 1 to 3.) However, maneuverability at high angles of attack can be limited because of degraded stability characteristics and inadequate aerodynamic control power.

Techniques for producing large control forces and moments by redirecting the engine exhaust flow (thrust vectoring) have been extensively investi-

gated over the past 13 years at the NASA Langley Research Center (ref. 4). Thrust vectoring provides large control moments that are independent of angle of attack by producing a component of thrust perpendicular to the body longitudinal axis. In an attempt to provide thrust-vectoring capability with minimum adverse impact on nozzle and aircraft performance, many vectoring concepts have been considered (refs. 4 to 13). In particular, both axisymmetric and nonaxisymmetric nozzles have been studied. These studies have emphasized nonaxisymmetric nozzles because their geometry permits more versatility of vectoring methods, including divergent flap deflection, sidewall variable geometry, blocker doors, plug vectoring, or postexit vanes. Nonaxisymmetric vectoring nozzles have almost exclusively utilized divergent flap deflection to achieve pitch thrust vectoring. This is because of the high flow-turning capability and low resultant thrust losses that have been measured during experimental investigations of this pitch-vectoring concept (ref. 4). Early investigations of thrust-vectoring nozzles were

limited to pitch vectoring only; however, recent studies have focused on multiaxis thrust-vectoring nozzles. Results show that, in some cases, performance in one of the vectoring directions is compromised by the devices needed to provide vectoring in the other direction. For instance, physical interference between pitch- and yaw-vectoring devices can limit the range of available multiaxis vector angles. In an attempt to alleviate these problems, a multiaxis thrust-vectoring nozzle was designed to vector the flow in pitch by deflection of the divergent flaps and in yaw by deflection of flow deflectors installed within the divergent flaps.

To evaluate the internal performance of this multiaxis thrust-vectoring nozzle, an investigation was conducted at static (wind-off) conditions in the static test facility of the Langley 16-Foot Transonic Tunnel. The model geometric parameters investigated were pitch vector angle, yaw vector angle, sidewall length, sidewall deflection, and nozzle expansion ratio. High-pressure air was used to simulate the jet exhaust flow at nozzle pressure ratios from 2.0 to approximately 13.0.

Symbols

All forces and moments (with the exception of resultant thrust) are referred to the model center-line (body axis). The model (balance) moment reference center was located at station 29.39. A discussion of the data reduction procedure and definitions of the force and moment terms and the propulsion relationships used herein can be found in reference 14.

A_e	nozzle exit area, in ²
A_t	nozzle throat area, in ²
b	total length of nozzle from attachment face to exit (see fig. 3(a)), in.
c	total length of nozzle sidewall (see fig. $5(a)$), in.
F	measured thrust along body axis, positive in forward direction, lbf
F_i	ideal isentropic gross thrust, lbf, $w_p \sqrt{\frac{R_j T_{t,j}}{g^2} \frac{2\gamma}{\gamma - 1}} \left[1 - \left(\frac{p_a}{p_{t,j}} \right)^{(\gamma - 1)/\gamma} \right]$
F_n	measured normal force, lbf
F_r	resultant thrust, lbf, $\sqrt{F^2 + F_n^2 + F_s^2}$
F_s	measured side force, positive to right when looking upstream, lbf

g	acceleration due to gravity, 32.174 ft/sec^2
h	height of nozzle exit (see fig. 3(a)), in.
L_f	length of divergent flap (see fig. $3(a)$), in.
NPR	nozzle pressure ratio, $\frac{p_{t,j}}{p_a}$
NPR_d	design nozzle pressure ratio (NPR for fully expanded flow at nozzle exit)
p	local static pressure, psi
p_a	ambient pressure, psi
$p_{t,j}$	average jet total pressure, psi
R_j	gas constant (for $\gamma = 1.3997$), 1716 ft ² /sec ² -°R
$T_{t,j}$	jet total temperature, °R
w_{i}	ideal isentropic weight-flow rate (for NPR > 1.89), lbf/sec,
	$A_t p_{t,j} \left(\frac{2}{\gamma+1}\right)^{\frac{\gamma+1}{2(\gamma-1)}} \sqrt{\frac{\gamma g^2}{T_{t,j} R_j}}$
w_p	measured weight-flow rate, lbf/sec
w_{t}	nominal nozzle throat width, 4.0 in.
X_s	linear nozzle dimension measured along centerline from throat to tip of sidewall (see fig. 3(a)), in.
x	linear nozzle dimension measured along centerline from throat to exit, used to define location of static pressure taps (see fig. 6), in.
y	lateral distance measured from model centerline, positive to right

model centerline, positive to right when looking upstream, used to define location of static pressure taps (see fig. 6(a)), in. ratio of specific heats, 1.3997 for air γ δ_{deff} deflector rotation angle as viewed along deflector hingeline (see fig. 4(b)), deg resultant pitch thrust vector angle, δ_p measured from nozzle centerline, positive deflection downward, $\tan^{-1}(F_n/F)$, deg $\delta_{v,p}$ geometric vector angle in pitch plane, measured from centerline, positive deflection downward, deg

 δ_y resultant yaw thrust vector angle,

measured from nozzle centerline, positive deflection to left when looking upstream, $\tan^{-1}(F_s/F)$,

deg

 θ sidewall deflection angle (see

fig. 5(b), deg

Abbreviations:

C-D convergent-divergent

Sta. model station, in.

Test Facility

This investigation was conducted in the static test facility of the Langley 16-Foot Transonic Tunnel. Testing is conducted in a large room where the jet from a single-engine propulsion simulation system exhausts to the atmosphere through an acoustically treated exhaust passage. A control room is remotely located from the test room, and a closed-circuit television is used to observe the model when the jet is operating. The static test facility has an air control system that is similar to that of the 16-Foot Transonic Tunnel and includes valving, filters, and a heat exchanger to maintain the jet flow at a constant stagnation temperature. The air system utilizes the same clean, dry air supply as that used by the 16-Foot Transonic Tunnel (ref. 15).

Single-Engine Propulsion Simulation System

A cutaway sketch of the single-engine propulsion simulation system on which various nozzle configurations were tested is presented in figure 1. The propulsion simulation system is shown with a typical nozzle configuration installed.

An external high-pressure air system supplies the propulsion simulation system with a continuous flow of clean, dry air at a constant stagnation temperature of about 540°R. This high-pressure air was varied during the jet simulation up to about 190 psi in the nozzle. As shown in figure 1, the high-pressure air was brought by six air lines through a support strut into an annular high-pressure plenum. The air was then discharged radially into a low-pressure plenum through eight equally spaced, multiholed sonic nozzles. This flow transfer system was designed to minimize any forces imposed by the transfer of axial momentum as the air is passed from the nonmetric high-pressure plenum to the metric (attached to the balance) low-pressure plenum. Two flexible metal bellows act as seals between the nonmetric and metric portions of the model and compensate for axial forces caused by pressurization. The air then passed through a circular-to-rectangular transition section, a rectangular choke plate (primarily used for flow straightening), a rectangular instrumentation section, and then through the nozzle, which exhausts to atmospheric pressure. The instrumentation section had a ratio of flow path width to height of 1.437 and was identical in geometry to the nozzle airflow entrance (nozzle connect station). All nozzle configurations tested were attached to the instrumentation section at model station 41.13.

Nozzle Design and Models

Nozzle Concept

The nonaxisymmetric convergent-divergent (C-D) nozzle was designed to vector the flow in pitch by simultaneous deflection of divergent flaps and in yaw by deflection of flat flow deflectors from the inner surface of the divergent flaps. The goal of the design was to add efficient yaw-vectoring capability to a pitch-vectoring nonaxisymmetric C-D nozzle while minimizing the effect of one vectoring mechanism on the other. The basic nozzle components consist of symmetric pairs (upper and lower) of convergent and divergent flaps and flat (internally) sidewalls to contain the exhaust flow in the lateral direction. Both nozzle convergent flaps pivot at the same model station (upstream of the throat) to allow changes in the throat area A_t . The divergent flaps pivot about a hingeline at the nozzle throat to allow variation of both the exit area A_e and the geometric pitch thrust vector angle $\delta_{v,p}$. Two yaw deflectors are located in each divergent flap (one on the left side and one on the right) and are stowed flat against the flap when no yaw thrust vectoring is desired. Each deflector is hinged along a line across the flow path that runs from the sidewall at the throat to the nozzle centerline near the exit. To produce yaw vectoring, the deflectors are deployed in pairs, one in the upper flap and one in the lower flap, on the same side of the nozzle. The angle of rotation of the deflectors δ_{defl} can be varied from 0° to 90° (relative to the divergent flap) to give a range of yaw vector angles δ_{y} .

Nozzle Models

A model of this nozzle concept was built and is shown in the photographs of figure 2 and in the sketches of figures 3 through 6. The nozzle model attached to the propulsion simulation system at model station 41.13 and had a constant flow path width of 4.0 in. Parametric nozzle geometry changes were made by combining various interchangeable upper and lower flaps, sidewalls, and yaw deflectors. The

specifications for each nozzle configuration tested during this investigation are presented in table 1.

The model consisted of baseline (unvectored) 1.8 and 2.3 expansion ratio A_e/A_t nozzles with corresponding design nozzle pressure ratios NPR_d of 8.8 and 13.6, respectively. The nozzles were designed with cutback sidewalls that were 70 percent $(X_s/L_f=0.70)$ of the divergent flap length. A geometric pitch thrust vector angle $\delta_{v,p}$ of 20° was tested for the 1.8 expansion ratio nozzle to study nozzle performance during multiaxis thrust vectoring. Since the pitch thrust-vectoring capability of nonaxisymmetric C-D nozzles has been extensively studied in previous investigations (refs. 7 and 8), only a brief study of pitch vectoring was undertaken in the current investigation.

Yaw-vectoring performance was extensively studied during this investigation. Because of the symmetry of the nozzle, yaw thrust vectoring was only investigated in the positive (to the left, looking upstream) δ_y direction. The nozzle was tested with yaw deflectors positioned at hingeline angles (the angle between the hingeline and the sidewall) of 27° and 34°. For each hingeline angle, a set of deflectors was designed that would completely block the right side of the 1.8 expansion ratio nozzle. The result was a set of tall deflectors along the 34° hingeline and a set of medium deflectors along the 27° hingeline. To investigate the effect of deflector height on yaw-vectoring performance, an additional set of deflectors was designed. This set of deflectors, arbitrarily placed at the 34° hingeline angle, was the shortest of the three and was designed to completely block the right side of a 1.3 expansion ratio nozzle. The fact that each deflector was designed for full blockage at a different geometric condition resulted in the differences in geometry between each deflector height. Deflector rotation angles tested were 0°, 30°, 45°, 60°, and 90° for the short deflectors and 0°, 30°, 60°, and 90° for the medium and tall deflectors. Figure 4 contains specifications of the yaw deflectors and shows their installation in the divergent flaps. In figure 4(a), dark shading represents the portion of the yaw deflectors that comes in contact with the exhaust flow (wetted surfaces), while light shading represents portions of the yaw deflectors that do not contact the exhaust flow (nonwetted surfaces).

Modifications to the nozzle sidewalls were investigated as means to provide exhaust flow relief and increase yaw-vectoring performance. The first modification consisted of increasing the cutback on the left and right sidewalls by reducing the sidewall length from 70 percent to 55 percent of the divergent flap length. The second modification consisted of hinging

the 70-percent sidewall at the throat and deflecting it outboard during yaw vectoring. For the 55-percent sidewall, it was hypothesized during the model design phase that the cutback would provide enough exhaust flow relief during yaw vectoring that outboard deflection of the sidewall would not be needed. The right sidewall remained at 0° at all times during this investigation. Sidewall cutback, deflector hingeline angle, and deflector height each represent a different nozzle design. All other model parameters investigated $(A_e/A_t, \delta_{\text{defl}}, \theta, \text{ and } \delta_{v,p})$ represent geometric variations that would be obtained on actual full-scale hardware through variable geometry.

Instrumentation

The weight-flow rate of high-pressure air to the nozzle was calculated from pressure and temperature measurements in a calibrated venturi system upstream of the high-pressure plenum. This venturi system is the standard high-pressure airflow measurement system in the static test facility. Forces and moments were measured by a six-component straingauge balance located on the nozzle centerline. Jet total pressure was measured at a fixed station in the instrumentation section by means of a four-probe rake through the upper surface, a three-probe rake from the side, and a three-probe rake through the corner. (See fig. 1.) An iron-constantan thermocouple was positioned in the instrumentation section to measure the jet total temperature.

Internal (jet flow) static pressure distributions were measured for selected model configurations. Static pressure orifice locations on the model are shown in figure 6. Three rows of internal static pressure orifices were located on the upper and lower flaps (fig. 6(a)), and one row was located on each sidewall (fig. 6(b)).

Data Reduction

Each data point is the average steady-state value computed from 50 frames of data taken at a rate of 10 frames per second. All data were taken in ascending order of $p_{t,j}$. With the exception of resultant thrust F_r , all data in this report are referenced to the model centerline (x-axis). Five basic nozzle internal performance parameters are used in the presentation of results; they are internal thrust ratio F/F_i , resultant thrust ratio F_r/F_i , discharge coefficient w_p/w_i , and two resultant thrust vector angles: δ_p for pitch and δ_y for yaw. A detailed description of the procedures used for data reduction in this investigation can be found in reference 14.

The internal thrust ratio F/F_i is the ratio of the measured nozzle thrust along the body axis to the

ideal nozzle thrust. Ideal thrust F_i is based on measured weight flow w_p , jet total pressure $p_{t,j}$, and jet total temperature $T_{t,j}$. (See the section "Symbols".) The balance axial-force measurement, from which the measured nozzle thrust F is subsequently obtained, is initially corrected for model weight tares and balance component interactions. Although the bellows arrangement in the air pressurization system was designed to minimize forces on the balance caused by pressurization, small bellows tares on the six-component balance still exist. These tares result from a small pressure difference between the ends of the bellows when air system internal velocities are high and from small differences in the spring constant of the forward and aft bellows when the bellows are pressurized. These bellows tares were determined by running Stratford choke calibration nozzles with known performance over a range of expected internal pressure and external forces and moments. The resulting tares were then applied to the six-component balance data obtained during the current investigation. Balance axial force obtained in this manner is a direct measurement of the thrust along the body axis. The procedure for computing the bellows tares is discussed in detail in reference 14.

The resultant thrust ratio F_r/F_i is the resultant thrust divided by the ideal isentropic thrust. Resultant thrust is obtained from the measured axial, normal, and side components of the jet resultant force. From the definitions of F and F_r , it is obvious that the thrust along the body axis F includes a reduction in thrust that results from turning the exhaust vector away from the axial direction, whereas the resultant thrust F_r does not. Losses included in both terms are the result of friction and pressure drags associated with the vectoring hardware and any changes in nozzle internal geometry associated with the hardware.

The nozzle discharge coefficient w_p/w_i is the ratio of measured weight-flow rate from upstream venturi measurements to ideal weight-flow rate, which is calculated from total-pressure and total-temperature measurements and the nozzle throat area. Nozzle throat area A_t is the measured geometric minimum area in the nozzle. This discharge coefficient is a measure of the nozzle efficiency in passing weight flow. The discharge coefficient is reduced by any momentum and vena contracta losses (effective throat area less than A_t).

The resultant thrust vector angles δ_p and δ_y are effective angles at which the thrust-vectoring mechanism turns the exhaust flow from the axial direction. As indicated in the section "Symbols," determination of these angles requires the measurement of axial, normal, and side forces on the model.

Presentation of Results

The results of this investigation are presented in both tabular form and plotted form. Table 1 is a description of the model configurations tested. The basic nozzle internal performance data for each configuration of this investigation are presented in table 2. Nozzle internal static pressure ratios $p/p_{t,j}$ are given in tables 3 to 38 for selected model configurations. Pressure data were not recorded during testing for configurations 7, 17, 24, 32, and 37. Dashed lines in plots of nozzle internal static pressure ratios represent either suspected separated flow data or possible curve fairings through missing data points. During discussion of results, comparisons of nozzle internal performance are made in terms of percentage change from isentropic conditions.

Comparison and summary plots for selected configurations are presented in figures 7 to 19 as follows:

	Fig	gure
Baseline (unvectored) nozzle performance with $X_s/L_f=0.70$ showing—		
Static performance characteristics	•	. 7
Internal static pressure distributions		. 8
Yaw-vectoring performance with $\delta_{v,p} = 0^{\circ}$ showing—		
Effect of deflector angle on nozzle performance. $A_e/A_t=1.8; X_s/L_f=0.70; \theta=0^{\circ}$. 9
Effect of deflector angle on static pressure distributions. $A_e/A_t=1.8; X_s/L_f=0.70; \theta=0^{\circ}$		10
Effect of deflector height on nozzle performance. $A_e/A_t=1.8; X_s/L_f=0.70; \theta=0^{\circ}$		11
Effect of expansion ratio on nozzle performance. $X_s/L_f = 0.70$; $\theta = 0^{\circ}$		12
Effect of sidewall modifications on nozzle performance. $A_e/A_t = 1.8$		13
Effect of NPR on static pressure distributions. $A_e/A_t = 1.8$; $X_s/L_f = 0.70$; $\theta = 0^\circ$; $\delta_{\text{defl}} = 0^\circ$		14
Effect of sidewall modifications on static pressure distributions. $A_e/A_t = 1.8$		15

Pitch-vectoring performance with $A_e/A_t = 1.8$, $X_s/L_f = 0.70$, $\delta_{\text{defl}} = 0^{\circ}$, and $\theta = 0^{\circ}$ showing—	
Effect of pitch vectoring on nozzle performance	16
Effect of pitch vectoring on static pressure distributions	17
Multiaxis thrust-vectoring performance with $A_e/A_t = 1.8$ and $X_s/L_f = 0.70$ showing—	
Effect of pitch vectoring on yaw-vectoring performance. $\delta_{\text{defl}} = 45^{\circ}$; $\theta = 0^{\circ}$	18
Effect of vaw vectoring on pitch-vectoring performance $\delta_{n,n} = 20^{\circ}$	1.9

Results and Discussion

Baseline Nozzle Performance

The internal performance characteristics of the baseline nozzles $(A_e/A_t = 1.8 \text{ and } 2.3)$ are presented in figure 7. The internal thrust ratio F/F_i , resultant thrust ratio F_r/F_i , discharge coefficient w_p/w_i , resultant pitch vector angle δ_p , and resultant yaw vector angle δ_y are shown as a function of nozzle pressure ratio. The 1.8 expansion ratio nozzle produced peak internal thrust ratios of approximately 0.99 near the design nozzle pressure ratio (NPR_d = 8.8). Thrust losses at nozzle pressure ratios below and above NPR_d are associated with nozzle overexpansion and underexpansion, respectively. Unfortunately, because of model balance limitations, the design nozzle pressure ratio (NPR_d = 13.6) was not reached for the 2.3 expansion ratio nozzle. However, based on previous studies of nonaxisymmetric convergentdivergent nozzles, it is expected that any differences in peak internal thrust ratio between the 1.8 and 2.3 expansion ratio nozzles would be small (ref. 7). There was no significant effect of nozzle expansion ratio on discharge coefficient. In a convergent-divergent nozzle, discharge coefficient is a function of nozzle geometry upstream of, and at, the nozzle throat. Any changes in nozzle geometry downstream of the throat, such as varying exit area A_e to vary expansion ratio A_e/A_t , would not be expected to affect discharge coefficient.

In general, the basic data show trends that are consistent with previous studies of C-D nozzles (refs. 7 to 13). One trend is the occurrence of two distinct local peaks in the performance curves (F/F_i) and F_r/F_i) of high-expansion-ratio nozzles; one occurs at high NPR and one occurs at low NPR. (See fig. 7.) The peak at high NPR occurs near the design nozzle pressure ratio where the exhaust nozzle is operating at optimum (fully expanded at the nozzle exit) conditions. The other peak occurs at low NPR where separation of the internal exhaust flow probably occurs in the divergent section of the nozzle. Consequently, multiple peaks in the performance curves are usually only seen for high-expansion-ratio nozzles, which, because of the large divergence angle, are the most susceptible to separation. Exhaust flow

separation from nozzle divergent flaps often produces locally higher thrust ratio performance at static conditions than at forward speeds by providing a lower effective nozzle expansion ratio. It should be noted that this beneficial effect may not exist at forward speeds where the external flow could aspirate the separated portion of the divergent flaps, causing increased drag and reduced thrust minus drag. If exhaust flow separation indeed increases thrust ratio, then exhaust flow reattachment to the divergent flap would decrease thrust ratio and produce the local peak in the performance curves that occurs for the high-expansion-ratio nozzle in figure 7. Similar results are documented in reference 9, where separation caused multiple peaks in the performance curves of a high-expansion-ratio nozzle.

During nonvectoring conditions $(\delta_{v,p} = 0^{\circ})$ and $\delta_{\text{defl}} = 0^{\circ}$, it would be expected that values of resultant pitch (δ_p) and yaw (δ_y) thrust vector angle would be zero. However, at low NPR resultant pitch vector angles of as much as 10° were recorded for the 2.3 expansion ratio nozzle. The variation in δ_p for the high-expansion-ratio nozzle is at nozzle pressure ratios in the same range as the performance peak discussed previously, where flow separation on the divergent flaps probably occurred. The separation is obviously asymmetric from the top flap to bottom flap in order to produce nonzero values of δ_p .

The effects of nozzle pressure ratio on the internal static pressure distributions of the baseline nozzles are presented in figures 8(a), (b), and (c) for nozzle pressure ratios of 2.0, 4.0, and 6.0, respectively. Although the pressure instrumentation inside the nozzle was sparse, it appears that the actual nozzle throat (sonic condition at $p/p_{t,j} = 0.528$) is downstream of the nozzle geometric throat (x = 0). This is most likely the result of a local flow separation bubble that forms just aft of the nozzle throat and reduces the effective throat area. For a nozzle pressure ratio of 2.0 (fig. 8(a)), increasing the nozzle expansion ratio increased flow separation along the divergent flap. The increase in separation at conditions below the design nozzle pressure ratio increased local static pressures in the separated region and effectively decreased the nozzle expansion ratio. This

increases thrust efficiency and results in a local peak in the performance curves of the 2.3 expansion ratio nozzle, as discussed previously. At higher nozzle pressure ratios (figs. 8(b) and (c)), flow separation has either moved downstream of the last static pressure tap or has been eliminated completely in the nozzle. This behavior of the actual nozzle throat is consistent with previous studies of nonaxisymmetric C-D nozzles (ref. 7).

Yaw-Vectoring Performance

The effect of deflector rotation angle δ_{defl} on nozzle internal performance characteristics is shown in figures 9(a), (b), and (c) for nozzles with short, medium, and tall deflectors, respectively. Depending on δ_{defl} and configuration, rotation of the yaw deflectors produced resultant yaw vector angles up to 21° that were controllable by varying yaw deflector rotation. Assuming the yawing moments produced on an aircraft by these devices would be proportional to yaw vector angle and throttle setting, this observation indicates that the yaw deflectors could be used as an effective aircraft control.

Yaw deflector rotation generally resulted in significant losses in both internal thrust ratio F/F_i and resultant thrust ratio F_r/F_i . The losses experienced in F/F_i were expected, since a portion of the exhaust flow is turned away from the axial direction by the yaw deflectors. The losses in F_r/F_i are a direct result of deploying the yaw deflectors into the supersonic jet-exhaust flow. Previous studies have shown that supersonic flow turning is an inefficient process because of oblique shocks that are formed in the divergent section of the nozzle (ref. 10). It is important to note that the magnitude of these turning losses did not always increase with increasing δ_{defl} . In fact, at low NPR, the deflectors deployed at 90° provided higher resultant thrust ratios than the deflectors at 60°. (See figs. 9(b) and (c), for example.) Two possible explanations exist for this behavior. First, as δ_{defl} is increased to higher values, the nozzle throat starts to shift downstream in the nozzle. This effect can be noted in the pressure distributions of figure 10. Simultaneously, blockage by the deflectors near the nozzle exit creates a lower effective exit area. The net effect of these phenomena is a lower effective expansion ratio and a lower effective NPR_d for the higher values of δ_{defl} . Thus, overexpansion losses are reduced at lower NPR, and underexpansion losses are increased at higher NPR, resulting in a shift in the peak F_r/F_i value to a lower NPR. Second, as the throat shifts downstream, the deflectors are operating in a larger region of subsonic flow, resulting in smaller supersonic flow turning losses. For the medium deflector, the throat is shifted only for the $\delta_{\text{defl}} = 90^{\circ}$ configuration. (See fig. 10(a).) This shift is substantiated by the change in discharge coefficient. Peak F_r/F_i for this configuration occurs at NPR = 4.0, which would indicate an effective expansion ratio for this configuration of about 1.2 rather than 1.8. For the tall deflector, the throat is shifted for the $\delta_{\text{defl}} = 60^{\circ}$ and 90° configurations. (See fig. 10(b).) The throat is shifted beyond the last pressure orifice for the $\delta_{\text{defl}} = 90^{\circ}$ configuration and may well be shifted all the way to the nozzle exit. A shift of this magnitude would change the nozzle from a C-D nozzle to a convergent $(A_e/A_t=1.0)$ nozzle. Shifts in the throat location, especially for the $\delta_{\text{defl}} = 90^{\circ}$ configuration, are again indicated by the discharge coefficient data. (See fig. 9(c).) The $\delta_{\text{defl}} = 60^{\circ}$ configuration has F_r/F_i trends similar to a single expansion ramp nozzle (ref. 11) in that it appears to have two F_r/F_i performance peaks. The first performance peak occurs at NPR = 3.0, which indicates an effective expansion ratio of about 1.090. The $\delta_{\text{defl}} = 90^{\circ}$ configuration has an F_r/F_i peak at about NPR = 2.0, which indicates an effective expansion ratio of about 1.002; this is only slightly higher than that for a convergent nozzle $(A_e/A_t = 1.0)$. Thus, the exhaust flow inside this nozzle configuration is subsonic except for possibly a small region of supersonic flow near the nozzle exit. Because of lower overexpansion losses at low NPR for the $\delta_{\text{defl}} = 90^{\circ}$ configuration (effective expansion ratio of about 1.002 versus 1.090 for the $\delta_{\text{defl}} = 60^{\circ}$ configuration) and lower supersonic flow turning losses, the resultant thrust ratios are higher for the $\delta_{\text{defl}} = 90^{\circ}$ configuration than those for the $\delta_{\text{defl}} = 60^{\circ} \text{ configuration.}$

Losses in nozzle discharge coefficient occurred at a deflector rotation angle of 60° for nozzles with tall deflectors and at a deflector rotation angle of 90° for nozzles with medium and tall deflectors. Losses in w_p/w_i ranged from 0 to 4 percent for the $\delta_{\text{defl}} = 60^{\circ}$ cases and up to 20 percent when the tall deflectors were deployed at 90°. These losses in w_p/w_i for the yaw-vectored configurations were caused by a shift in the physical throat location from a location near the geometric throat to a position farther down the divergent flap. This is demonstrated by the pressure plots in figure 10 where a shift in the physical throat location is indicated by the static pressure measurements. Therefore, the effective throat area is smaller than the geometric unvectored throat area used to compute ideal weight-flow rate. Since a reduction in throat area reduces the ability of a nozzle to pass weight flow at a given nozzle pressure ratio, the discharge coefficient decreased.

The effect of yaw deflector height is summarized in figure 11 for the 1.8 expansion ratio nozzles. The internal thrust ratio, resultant thrust ratio, discharge coefficient, resultant pitch vector angle, and resultant yaw vector angle are plotted as a function of the deflector rotation angle at a constant nozzle pressure ratio. In general, the medium deflectors provided the best overall performance by providing the largest resultant yaw vector angles with the least losses in thrust ratios. Compared with the medium deflector, the losses in F_r/F_i for the tall and short deflectors were greater by 6 percent and 2 percent, respectively. The effect of varying the deflector height on resultant yaw vector angles was generally small. The maximum deviation in resultant yaw vector angle between the deflector heights was less than 3°. At deflector rotation angles less than 60°, the effect of deflector height on discharge coefficient was small. However, as discussed previously, the nozzles with tall deflectors suffered substantial losses in discharge coefficient at $\delta_{\text{defl}} = 90^{\circ}$.

The effects of expansion ratio on nozzle internal performance characteristics are summarized in figures 12(a) and (b) for nozzle pressure ratios of 4.0 and 6.0, respectively. During yaw-vectored operation, increasing the nozzle expansion ratio increased the nozzle discharge coefficient at deflector rotation angles of 90° while having little effect on the resultant yaw vector angles generated. For the 2.3 expansion ratio nozzle, the nozzle exit area has been increased by rotating the nozzle divergent flap trailing edges outward. Thus, for a constant value of δ_{deff} , the deflectors do not present as large a flow blockage as for the 1.8 expansion ratio nozzle. The 1.8 expansion ratio configuration generally had higher F_r/F_i performance than the 2.3 expansion ratio configuration because, at the NPR shown, it was operating closer to the design NPR (or effective NPR_d) than the 2.3 expansion ratio configuration and thus had lower overexpansion losses.

The effects of sidewall modifications on the internal performance and thrust-vectoring capability of the 1.8 expansion ratio nozzle are presented in figures 13 to 15. As mentioned previously, two sidewall modifications were investigated as means to increase yaw-vectoring performance. The first modification consisted of increasing the sidewall cutback by reducing sidewall length from 70 percent to 55 percent of the divergent flap length. The second modification consisted of hinging the 70-percent sidewall at the nozzle throat and deflecting it outboard during yaw vectoring.

The effects of sidewall cutback and deflection on nozzle internal performance characteristics are presented in figure 13 for nozzles with tall deflectors. As mentioned previously, the intent of sidewall cutback was to provide exhaust flow relief during yaw vectoring and, therefore, increase yaw-vectoring performance. The results indicate that sidewall cutback effects on nozzle performance were negligible at deflector rotation angles of 0° and 30°. However, at deflector rotation angles of 60° and 90°, increases in resultant thrust ratio, discharge coefficient, and resultant yaw vector angle occurred as a result of increasing the sidewall cutback. At maximum deflector rotation angles ($\delta_{\text{defl}} = 90^{\circ}$), increasing the amount of sidewall cutback resulted in increases in F_r/F_i of 2 percent, in w_p/w_i of 3.5 percent, and in δ_y of as much as 8°. The change in discharge coefficient indicates that the actual throat area increased as a result of increasing the sidewall cutback. It is likely that this increase in throat area is due to a rotation, or skewing, of the throat plane in the positive δ_{y} direction that occurred as the sidewall cutback was increased. Skewing of the nozzle throat would account for the increase in yaw-vectoring performance observed. The increases in F_r/F_i that resulted from increasing the sidewall cutback were unexpected. It is possible that the flow relief provided by the cutback sidewall allowed the exhaust flow to expand more efficiently than it did for the nozzle with 70-percent sidewalls. Regardless of the reasons, it is obvious that the 55-percent sidewall configuration is the more efficient yaw-vectoring case.

During unvectored operation $(\delta_{\text{defl}} = 0^{\circ})$, outboard deflection of the left sidewall generally resulted in losses in resultant thrust ratio F_r/F_i . (See fig. 13(a).) This trend is similar to those shown in reference 12 for a nozzle with an outboard-deflecting sidewall. Basically, outboard deflection of a sidewall increases nozzle exit area and thus expansion ratio. Increased nozzle expansion ratio would move maximum nozzle performance to higher values of NPR (higher NPR_d), increase nozzle overexpansion losses at low NPR, and decrease nozzle underexpansion losses at high NPR. The deflected sidewall increased nozzle exit area to 8.112 in² and thus increased nozzle expansion ratio to 2.3. This resulted in a design nozzle pressure ratio of 13.6 for the deflected sidewall configuration versus 8.8 for the undeflected configuration. The deflected sidewall configuration generally followed the expected trends with the exception of NPR = 2.0. At NPR = 2.0, outboard sidewall deflection increased separation inside the nozzle. The effect of separation at NPR = 2.0 was to reduce the effective expansion ratio to a value below 1.8, thereby reducing overexpansion losses and increasing thrust performance. There was essentially

no effect of sidewall deflection on nozzle discharge coefficient. As discussed previously, discharge coefficient in a convergent-divergent nozzle is a function of nozzle geometry upstream of, and at, the nozzle throat. Therefore, changes in nozzle geometry downstream of the throat would not be expected to affect discharge coefficient.

The effect of sidewall deflection on yaw-vectoring performance is shown in figure 13(a). deflection produced negative yaw vector angles at NPR < 4.0, whereas positive yaw vector angles were generated at NPR > 4.0. Figure 14 shows the effect of NPR on internal static pressure distributions of the deflected sidewall configuration. As shown, static pressure distributions indicate that flow separation generally occurred on the deflected sidewall in a location that was NPR dependent. At NPR = 2.0. exhaust flow separation from the divergent flaps and sidewalls produced higher static pressure ratios $p/p_{t,i}$ on the left sidewall than on the right sidewall. The resulting pressure gradient between the left and right sidewalls generated negative sideforce $(-F_s)$. It also appears that the throat may be skewed to the right (farther downstream on the left sidewall than on the right), which would tend to vector flow opposite the desired direction. The combination of the skewed throat and the pressure gradient produced negative resultant yaw vector angles at low NPR. As NPR increased, the flow tended to stay attached farther down the sidewall, allowing expansion of the flow along the sidewall to lower static pressures. At NPR = 4.0, the combination of the pressure gradient and any vectored flow results in $\delta_y = 0^{\circ}$. At higher NPR, the flow continued to expand down the deflected sidewall to static pressure values lower than on the right sidewall. The resulting static pressure gradient between the left and right sidewalls generated positive sideforce (F_s) . The overall low resultant yaw vector angles at NPR > 4.0 indicate that little exhaust flow was actually turned by the deflected sidewall. This is consistent with reference 12, which indicates that exhaust flow has little tendency to expand (turn) out of an open sidewall at overexpanded nozzle conditions. Therefore, at NPR < 13.6, it would be expected that little flow turning would occur; any resultant vectoring would mainly be the result of pressure gradients inside the nozzle.

In actual practice, it is doubtful that an airplane would fly at an expansion ratio of 1.8 (or 2.3) at nozzle pressure ratios below NPR_d (unless nozzle geometry was fixed). For a variable-geometry nozzle, the expansion ratio would be set at the appropriate value so that the nozzle would be operating on de-

sign (near F_r/F_i peak). For example, at NPR = 4.0 the nozzle expansion ratio would be set to approximately 1.2. In all probability, a nozzle with this expansion ratio would not generate negative δ_y until a much lower NPR was reached. (See ref. 12.) For fixed nozzle geometry as tested, the opposite sidewall could be deflected to provide F_s in the desired direction at NPR < 4.0.

During yaw vectoring ($\delta_{\text{defl}} > 0^{\circ}$), combining sidewall deflection ($\theta = 25^{\circ}$) with deflector rotation angle at NPR > 4.0 (where the effects of θ and δ_{defl} are additive) produced the largest resultant yaw vector angles (up to 35°) while generally increasing F_r/F_i (at $\delta_{\text{defl}} > 30^{\circ}$). At $\delta_{\text{defl}} = 30^{\circ}$ (fig. 13(b)), deflecting the left sidewall increased resultant yaw vector angle by 5° at NPR_d while having little effect on thrust ratios or discharge coefficient. As δ_{defl} increases, the effectiveness of the deflected sidewall also increases. At $\delta_{\text{defl}} = 90^{\circ}$, deflecting the left sidewall outboard produced up to a 2.5-percent increase in F_r/F_i , a 12-percent increase in w_p/w_i , and a 17° increase in resultant yaw vector angle. (See fig. 13(d).) As mentioned previously, the nozzle throat shifted downstream at $\delta_{\text{defl}} = 90^{\circ}$. As indicated by the pressure plots in figure 15(d), the outboard deflection of the nozzle sidewall reduces the amount of downstream shift of the nozzle throat and thus yields the previously noted increase in discharge coefficient. Reducing the downstream shift allowed the nozzle to operate at a higher effective expansion ratio and a higher effective NPR_d . Thus, underexpansion losses were reduced at higher NPR and overexpansion losses were increased at lower NPR, resulting in a shift in the peak F_r/F_i value to a higher NPR.

Effects of Geometric Pitch Vector Angle

The effects of geometric pitch vector angle $\delta_{v,p}$ on the internal performance and thrust-vectoring capability of the 1.8 expansion ratio nozzles are presented in figures 16 to 19. Divergent flap deflection produced resultant pitch vector angles δ_p that, although dependent on nozzle pressure ratio for NPR < 4.0, were nearly equal to the geometric pitch vector angle at NPR > 4.0. (See fig. 16.) A maximum resultant pitch vector angle of 25° was measured at NPR < 4.0, where the nozzle was operating at highly overexpanded conditions. During pitch-vectored operation, an overexpansion occurs over much of the lower divergent flap, resulting in a pressure gradient between the upper and lower flaps (fig. 17). This pressure gradient tends to bias the flow toward the lower divergent flap. Because of the divergence angle, the angle of the lower divergent flap is greater than the geometric thrust vector angle, and resultant

pitch vector angles δ_p greater than $\delta_{v,p}$ are possible, especially at low NPR.

The effects of pitch thrust vectoring on resultant thrust ratios were generally small. This was expected, since previous studies have shown that divergent flap deflection is an efficient and effective method of producing pitch thrust vectoring in nonaxisymmetric C-D nozzles (ref. 4). Losses in nozzle discharge coefficient of approximately 2.5 percent occurred during pitch vectoring, probably because of a sharper throat corner on the lower divergent flap and shifting of the actual throat location on the upper divergent flap. The shift in the throat location is indicated by the static pressure distributions plotted in figure 17. Figure 17 also shows that a pressure correction occurs upstream of the throat in the pitchvectored configuration. This behavior may indicate a larger flow-separation bubble occurring in the pitchvectored configuration, resulting in a smaller effective throat area. As mentioned previously, a reduction in throat area leads to a reduction in nozzle discharge coefficient.

The effects of multiaxis thrust vectoring on the internal performance and thrust-vectoring capability of the 1.8 expansion ratio nozzles are presented in figures 18 and 19. Figure 18 presents the effects of pitch vectoring on yaw-vectoring performance with $\delta_{\text{defl}} = 45^{\circ}$ and $\theta = 0^{\circ}$. The results indicate that the addition of pitch vectoring has little effect on vaw-vectoring performance. The only significant loss to occur was the 2.5-percent drop in discharge coefficient that was previously associated with pitch vectoring. The effects of yaw vectoring on pitchvectoring performance with $\delta_{v,p} = 20^{\circ}$ are presented in figure 19. The results indicate that there is relatively little effect of δ_{defl} or θ on pitch-vectoring performance at NPR > 3.0. However, at NPR < 3.0, the addition of yaw vectoring reduced the resultant pitch vector angles by approximately 5°.

Conclusions

An investigation has been conducted in the static test facility of the Langley 16-Foot Transonic Tunnel to evaluate the internal performance of a nonaxisymmetric convergent-divergent nozzle with multiaxis thrust-vectoring capability. The goal of the design was to add efficient yaw-vectoring capability to a pitch-vectoring nonaxisymmetric convergent-divergent nozzle while minimizing the effect of one vectoring direction on the other. The test was conducted with no external flow, and nozzle pressure ratio was varied from 2.0 to approximately 13.0. The results of this investigation indicate the following conclusions:

- 1. Yaw deflectors installed in the divergent flaps of a pitch-vectoring nonaxisymmetric convergent-divergent nozzle were effective in generating resultant yaw vector angles up to 21° (with the baseline sidewall) that were controllable by varying yaw deflector rotation. During multiaxis (pitch and yaw) thrust vectoring, the effects of one vectoring direction on the other were generally small.
- 2. In general, the medium yaw deflectors had the best overall nozzle internal performance characteristics by providing the largest resultant yaw vector angles with the least losses in thrust ratios.
- 3. Losses in nozzle discharge coefficient during yaw thrust vectoring are the result of a shift in the physical throat location in the nozzle.
- 4. During unvectored operation, varying the sidewall cutback had little or no effect on nozzle internal performance. However, during yaw-vectored operation, increasing the sidewall cutback increased nozzle performance at deflector rotation angles of 60° and 90°.
- 5. During yaw vectoring, combining sidewall deflection with deflector rotation significantly increased nozzle internal performance.

NASA Langley Research Center Hampton, VA 23681-0001 July 6, 1993

References

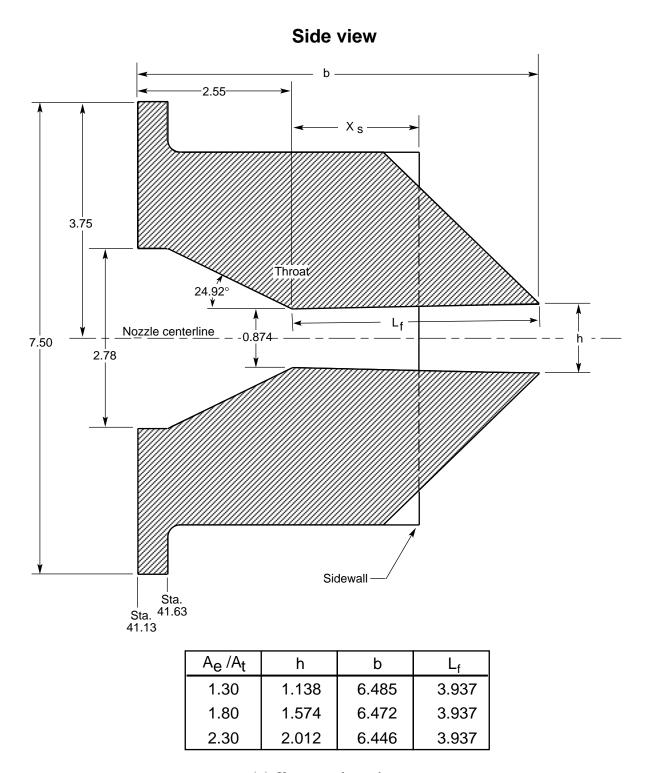
- Callahan, C. J.: Tactical Aircraft Payoffs for Advanced Exhaust Nozzles. AIAA-86-2660, Oct. 1986.
- Herbst, W. B.: Future Fighter Technologies. J. Aircr., vol. 17, no. 8, Aug. 1980, pp. 561–566.
- Nguyen, Luat T.; and Gilbert, William P.: Impact of Emerging Technologies on Future Combat Aircraft Agility. AIAA-90-1304, May 1990.
- Berrier, Bobby L.: Results From NASA Langley Experimental Studies of Multiaxis Thrust Vectoring Nozzles. SAE 1988 Transactions—Journal of Aerospace, Section 1—Volume 97, c.1989, pp. 1.1289–1.1304. (Available as SAE Paper 881481.)
- Berrier, Bobby L.; and Mason, Mary L.: Static Performance of an Axisymmetric Nozzle With Post-Exit Vanes for Multiaxis Thrust Vectoring. NASA TP-2800, 1988.
- Berrier, Bobby L.; and Taylor, John G.: Internal Performance of Two Nozzles Utilizing Gimbal Concepts for Thrust Vectoring. NASA TP-2991, 1990.

- Re, Richard J.; and Leavitt, Laurence D.: Static Internal Performance Including Thrust Vectoring and Reversing of Two-Dimensional Convergent-Divergent Nozzles. NASA TP-2253, 1984.
- 8. Taylor, John G.: Static Investigation of a Two-Dimensional Convergent-Divergent Exhaust Nozzle With Multiaxis Thrust-Vectoring Capability. NASA TP-2973, 1990.
- 9. Berrier, Bobby L.; and Re, Richard J.: Investigation of Convergent-Divergent Nozzles Applicable to Reduced-Power Supersonic Cruise Aircraft. NASA TP-1766, 1980.
- 10. Wing, David J.; and Asbury, Scott C.: Static Performance of a Cruciform Nozzle With Multiaxis Thrust-Vectoring and Reverse-Thrust Capabilities. NASA TP-3188, 1992.
- Berrier, Bobby L.; and Re, Richard J.: Effect of Several Geometric Parameters on the Static Internal Performance of Three Nonaxisymmetric Nozzle Concepts. NASA TP-1468, 1979.

- Mason, M. L.; and Berrier, B. L.: Static Investigation of Several Yaw Vectoring Concepts on Nonaxisymmetric Nozzles. NASA TP-2432, 1985.
- 13. Capone, Francis J.; Mason, Mary L.; and Leavitt, Laurence D.: An Experimental Investigation of Thrust Vectoring Two-Dimensional Convergent-Divergent Nozzles Installed in a Twin-Engine Fighter Model at High Angles of Attack. NASA TM-4155, 1990.
- 14. Mercer, Charles E.; Berrier, Bobby L.; Capone, Francis J.; and Grayston, Alan M.: Data Reduction Formulas for the 16-Foot Transonic Tunnel NASA Langley Research Center, Revision 2. NASA TM-107646, 1992.
- Staff of the Propulsion Aerodynamics Branch: A User's Guide to the Langley 16-Foot Transonic Tunnel Complex, Revision 1. NASA TM-102750, 1990. (Supersedes NASA TM-83186, compiled by Kathryn H. Peddrew, 1981.)

Table 1. Description of Model Configurations

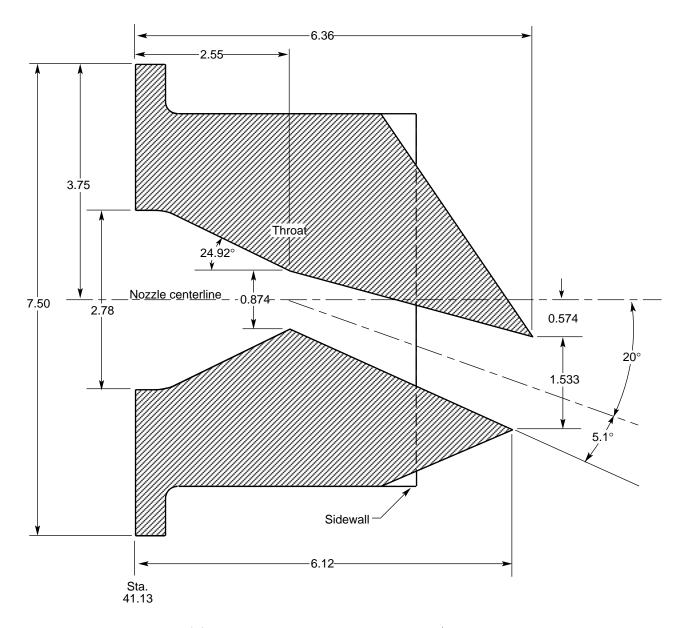
Configuration	A_e/A_t	A_t , in ²	NPR_d	$\delta_{v,p}, \deg$	X_s/L_f	θ , deg	δ_{defl} , deg	Deflector height
1	1.3	3.5312	4.6	0	0.55	0	0	Zero
2							30	Short
3							60	
4	\downarrow		↓ ↓				90	\downarrow
5	1.8		8.8				0	${ m Zero}$
6		,					30	Short
7		,					45	
8							60	
9							90	\downarrow
10							30	${f Medium}$
11							60	
12							90	\downarrow
13		,					30	Tall
14							60	
15		↓ ↓		\downarrow			90	\downarrow
16		3.4166		20			0	${ m Zero}$
17							45	Short
18							30	Tall
19	\downarrow	↓ ↓	↓ ↓	\downarrow			60	Tall
20	2.3	3.5312	13.6	0			0	${ m Zero}$
21							60	Tall
22	\downarrow		↓ ↓		↓		90	Tall
23	1.8		8.8		0.70		0	${ m Zero}$
24							45	Short
25							30	${ m Medium}$
26							60	
27							90	\downarrow
28							30	Tall
29		,					60	
30						↓ ↓	90	\downarrow
31						25	0	${ m Zero}$
32							45	Short
33							30	Tall
34							60	
35		↓		↓		↓	90	↓ ↓
36		3.4166		20		0	0	${ m Zero}$
37						0	45	Short
38	↓	↓	↓	↓		25	45	Short
39	2.3	3.5312	13.6	0		0	0	${ m Zero}$
40							60	Tall
41	↓	↓	↓	↓ ↓	↓	↓	90	Tall



(a) Unvectored nozzles.

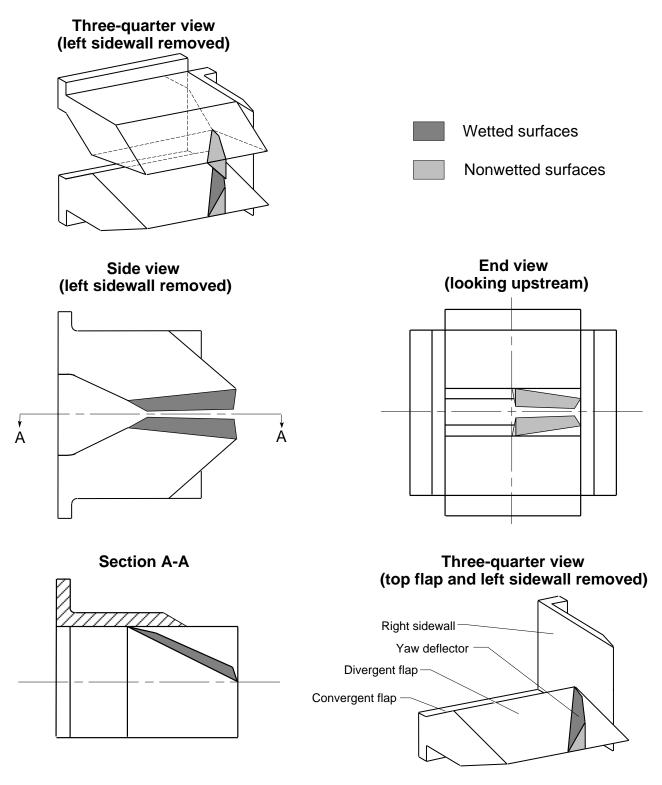
Figure 3. Internal nozzle geometry. All dimensions are in inches unless otherwise noted.

Side view



(b) Pitch-vectored nozzle, $\delta_{v,p}=20^{\circ},\,A_e/A_t=1.8.$

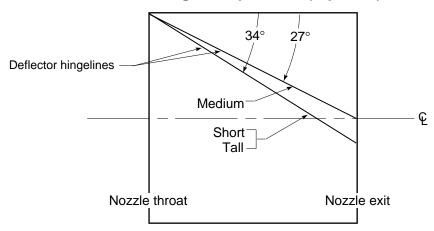
Figure 3. Concluded.



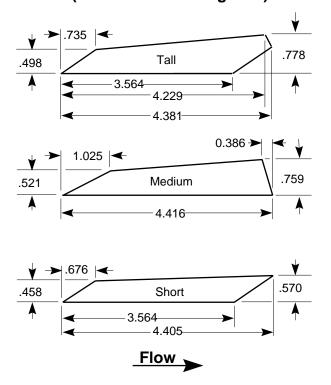
(a) Installation of medium yaw deflectors. $\delta_{\text{defl}} = 60^{\circ}.$

Figure 4. Static test model showing installation and details of deflector flaps. All dimensions are in inches unless otherwise noted.

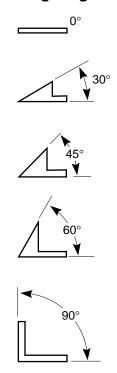
Divergent flap details (top view)



Deflector sizes and shapes (view normal to hingeline)

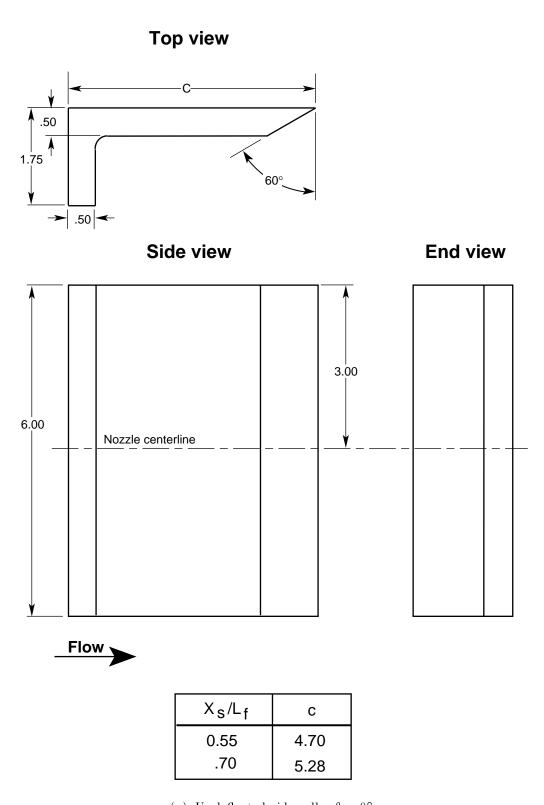


Deflector rotation angles, δ_{defl} (view along hingeline)



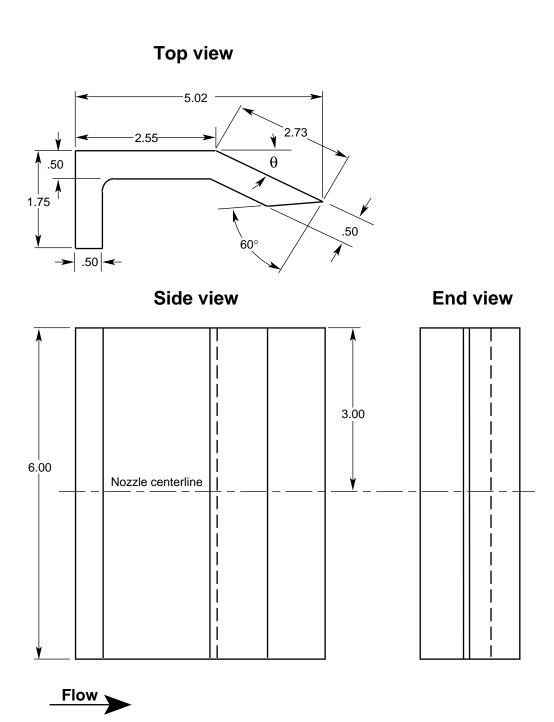
(b) Details of divergent flaps and yaw deflectors.

Figure 4. Concluded.



(a) Undeflected sidewalls. $\theta = 0^{\circ}$.

Figure 5. Nozzle sidewall geometry. All dimensions are in inches unless otherwise noted.

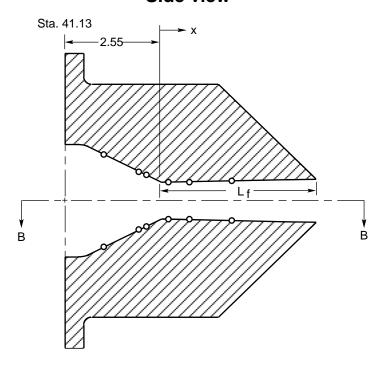


(b) Deflected sidewall. $\theta=25\,^{\rm o};\,X_s/L_f=0.70\,.$

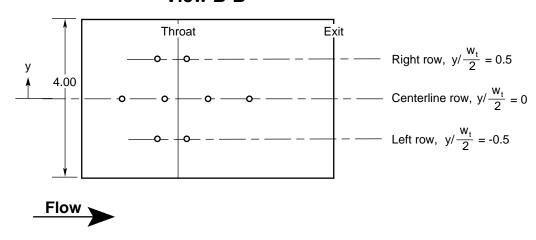
Figure 5. Concluded.

Static pressure orifice locations				
x, in.	Station, in.	x/L _f		
-1.45 55 35 .20 .75 1.85	42.23 43.13 43.33 43.88 44.43 45.53	-0.368 140 089 .051 .191 .470		

Side view



View B-B

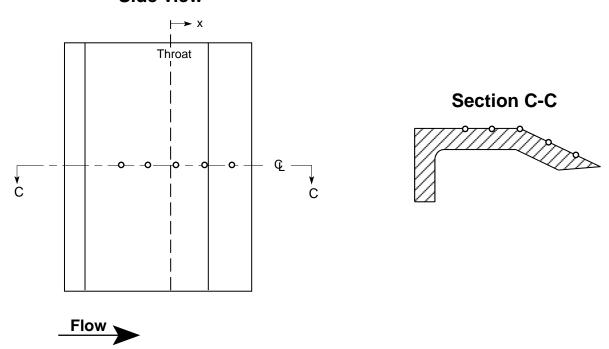


(a) Upper and lower flaps.

Figure 6. Nozzle static pressure orifice locations. All dimensions are in inches unless otherwise noted.

Static pressure orifice locations					
Side	wall	x, in.	Station, in.	x/L _f	
X _s /L _f	θ				
0.55	0°	-1.209 538 .133 .804 1.474 -1.041 287 .467 1.221 1.976 -1.041 287 .423 1.107 1.791	42.471 43.142 43.813 44.484 45.154 42.639 43.393 44.147 44.901 45.656 42.639 43.393 44.103 44.787 45.471	-0.307 137 .034 .204 .374 264 073 .119 .310 .502 264 073 .107 .281	

Side view



(b) Left and right sidewalls.

Figure 6. Concluded.

Figure 14. Effect of nozzle pressure ratio on internal static pressure distributions with $A_e/A_t=1.8$, $\delta_{v,p}=0^\circ$, $X_s/L_f=0.70$, $\theta=25^\circ$, and $\delta_{\text{defl}}=0^\circ$.

Table 2. Nozzle Performance Data

- Table 2. Continued
- Table 2. Concluded
- Table 3. Nozzle Internal Static Pressure Ratios $p/p_{t,j}$ for Configuration 1
 - (a) Upper and lower flap internal static pressure ratios
 - (b) Sidewall internal static pressure ratios
- Table 4. Nozzle Internal Static Pressure Ratios $p/p_{t,j}$ for Configuration 2
 - (a) Upper and lower flap internal static pressure ratios
 - (b) Sidewall internal static pressure ratios
- Table 5. Nozzle Internal Static Pressure Ratios $p/p_{t,j}$ for Configuration 3
 - (a) Upper and lower flap internal static pressure ratios
 - (b) Sidewall internal static pressure ratios
- Table 6. Nozzle Internal Static Pressure Ratios $p/p_{t,j}$ for Configuration 4
 - (a) Upper and lower flap internal static pressure ratios
 - (b) Sidewall internal static pressure ratios
- Table 7. Nozzle Internal Static Pressure Ratios $p/p_{t,j}$ for Configuration 5
 - (a) Upper and lower flap internal static pressure ratios

- (b) Sidewall internal static pressure ratios
- Table 8. Nozzle Internal Static Pressure Ratios $p/p_{t,j}$ for Configuration 6
 - (a) Upper and lower flap internal static pressure ratios
 - (b) Sidewall internal static pressure ratios
- Table 9. Nozzle Internal Static Pressure Ratios $p/p_{t,j}$ for Configuration 8
 - (a) Upper and lower flap internal static pressure ratios
 - (b) Sidewall internal static pressure ratios
- Table 10. Nozzle Internal Static Pressure Ratios $p/p_{t,j}$ for Configuration 9
 - (a) Upper and lower flap internal static pressure ratios
 - (b) Sidewall internal static pressure ratios
- Table 11. Nozzle Internal Static Pressure Ratios $p/p_{t,j}$ for Configuration 10
 - (a) Upper and lower flap internal static pressure ratios
 - (b) Sidewall internal static pressure ratios
- Table 12. Nozzle Internal Static Pressure Ratios $p/p_{t,j}$ for Configuration 11
 - (a) Upper and lower flap internal static pressure ratios
 - (b) Sidewall internal static pressure ratios
- Table 13. Nozzle Internal Static Pressure Ratios $p/p_{t,j}$ for Configuration 12
 - (a) Upper and lower flap internal static pressure ratios
 - (b) Sidewall internal static pressure ratios
- Table 14. Nozzle Internal Static Pressure Ratios $p/p_{t,j}$ for Configuration 13
 - (a) Upper and lower flap internal static pressure ratios
 - (b) Sidewall internal static pressure ratios
- Table 15. Nozzle Internal Static Pressure Ratios $p/p_{t,j}$ for Configuration 14
 - (a) Upper and lower flap internal static pressure ratios
 - (b) Sidewall internal static pressure ratios
- Table 16. Nozzle Internal Static Pressure Ratios $p/p_{t,j}$ for Configuration 15
 - (a) Upper and lower flap internal static pressure ratios
 - (b) Sidewall internal static pressure ratios

- Table 17. Nozzle Internal Static Pressure Ratios $p/p_{t,j}$ for Configuration 16
 - (a) Upper and lower flap internal static pressure ratios

Table 17. Concluded

- (b) Sidewall internal static pressure ratios
- Table 18. Nozzle Internal Static Pressure Ratios $p/p_{t,j}$ for Configuration 18
 - (a) Upper and lower flap internal static pressure ratios

Table 18. Concluded

- (b) Sidewall internal static pressure ratios
- Table 19. Nozzle Internal Static Pressure Ratios $p/p_{t,j}$ for Configuration 19
 - (a) Upper and lower flap internal static pressure ratios
 - (b) Sidewall internal static pressure ratios
- Table 20. Nozzle Internal Static Pressure Ratios $p/p_{t,j}$ for Configuration 20
 - (a) Upper and lower flap internal static pressure ratios
 - (b) Sidewall internal static pressure ratios
- Table 21. Nozzle Internal Static Pressure Ratios $p/p_{t,j}$ for Configuration 21
 - (a) Upper and lower flap internal static pressure ratios
 - (b) Sidewall internal static pressure ratios
- Table 22. Nozzle Internal Static Pressure Ratios $p/p_{t,j}$ for Configuration 22
 - (a) Upper and lower flap internal static pressure ratios
 - (b) Sidewall internal static pressure ratios
- Table 23. Nozzle Internal Static Pressure Ratios $p/p_{t,j}$ for Configuration 23
 - (a) Upper and lower flap internal static pressure ratios
 - (b) Sidewall internal static pressure ratios
- Table 24. Nozzle Internal Static Pressure Ratios $p/p_{t,j}$ for Configuration 25
 - (a) Upper and lower flap internal static pressure ratios
 - (b) Sidewall internal static pressure ratios
- Table 25. Nozzle Internal Static Pressure Ratios $p/p_{t,j}$ for Configuration 26
 - (a) Upper and lower flap internal static pressure ratios

- (b) Sidewall internal static pressure ratios
- Table 26. Nozzle Internal Static Pressure Ratios $p/p_{t,j}$ for Configuration 27
 - (a) Upper and lower flap internal static pressure ratios
 - (b) Sidewall internal static pressure ratios
- Table 27. Nozzle Internal Static Pressure Ratios $p/p_{t,j}$ for Configuration 28
 - (a) Upper and lower flap internal static pressure ratios
 - (b) Sidewall internal static pressure ratios
- Table 28. Nozzle Internal Static Pressure Ratios $p/p_{t,j}$ for Configuration 29
 - (a) Upper and lower flap internal static pressure ratios
 - (b) Sidewall internal static pressure ratios
- Table 29. Nozzle Internal Static Pressure Ratios $p/p_{t,j}$ for Configuration 30
 - (a) Upper and lower flap internal static pressure ratios
 - (b) Sidewall internal static pressure ratios
- Table 30. Nozzle Internal Static Pressure Ratios $p/p_{t,j}$ for Configuration 31
 - (a) Upper and lower flap internal static pressure ratios
 - (b) Sidewall internal static pressure ratios
- Table 31. Nozzle Internal Static Pressure Ratios $p/p_{t,j}$ for Configuration 33
 - (a) Upper and lower flap internal static pressure ratios
 - (b) Sidewall internal static pressure ratios
- Table 32. Nozzle Internal Static Pressure Ratios $p/p_{t,j}$ for Configuration 34
 - (a) Upper and lower flap internal static pressure ratios
 - (b) Sidewall internal static pressure ratios
- Table 33. Nozzle Internal Static Pressure Ratios $p/p_{t,j}$ for Configuration 35
 - (a) Upper and lower flap internal static pressure ratios
 - (b) Sidewall internal static pressure ratios
- Table 34. Nozzle Internal Static Pressure Ratios $p/p_{t,j}$ for Configuration 36
 - (a) Upper and lower flap internal static pressure ratios

Table 34. Concluded

(b) Sidewall internal static pressure ratios

Table 35. Nozzle Internal Static Pressure Ratios $p/p_{t,j}$ for Configuration 38

- (a) Upper and lower flap internal static pressure ratios
 - (b) Sidewall internal static pressure ratios

Table 36. Nozzle Internal Static Pressure Ratios $p/p_{t,j}$ for Configuration 39

(a) Upper and lower flap internal static pressure ratios

Table 36. Concluded

(b) Sidewall internal static pressure ratios

Table 37. Nozzle Internal Static Pressure Ratios $p/p_{t,j}$ for Configuration 40

- (a) Upper and lower flap internal static pressure ratios
 - (b) Sidewall internal static pressure ratios

Table 38. Nozzle Internal Static Pressure Ratios $p/p_{t,j}$ for Configuration 41

- (a) Upper and lower flap internal static pressure ratios
 - (b) Sidewall internal static pressure ratios

Figure 1. Cutaway side view of single-engine propulsion simulation system with typical nozzle configuration installed. All dimensions are in inches unless otherwise noted.

L-88-6834

(a) Three-quarter view of configuration 19.

Figure 2. Photographs showing nozzle configurations 19, 37, and 30.

L-88-6840

(b) Side view of configuration 19.

Figure 2. Continued.

L-92-10789

(c) Side view of configuration 37; left sidewall removed.

Figure 2. Continued.

L-92-10792

(d) Side view of configuration 30; left sidewall removed.

Figure 2. Concluded.

- Figure 7. Static performance characteristics of baseline nozzles with $\delta_{v,p} = 0^{\circ}$, $X_s/L_f = 0.70$, $\theta = 0^{\circ}$, and $\delta_{\text{defl}} = 0^{\circ}$.
 - (a) Nominal NPR = 2.0.
- Figure 8. Internal static pressure distributions of baseline nozzles with $\delta_{v,p} = 0^{\circ}$, $X_s/L_f = 0.70$, $\theta = 0^{\circ}$, and $\delta_{\text{defl}} = 0^{\circ}$.
 - (b) Nominal NPR = 4.0.

Figure 8. Continued.

(c) Nominal NPR = 6.0.

Figure 8. Concluded.

(a) Short deflectors.

- Figure 9. Effect of deflector angle on nozzle internal performance characteristics with $A_e/A_t = 1.8$, $\delta_{v,p} = 0^{\circ}$, $X_s/L_f = 0.70$, and $\theta = 0^{\circ}$.
 - (b) Medium deflectors.

Figure 9. Continued.

(c) Tall deflectors.

Figure 9. Concluded.

- (a) Medium deflectors; nominal NPR = 4.0.
- Figure 10. Effect of deflector angle on internal static pressure distributions with $A_e/A_t=1.8$, $\delta_{v,p}=0^{\circ}$, $X_s/L_f=0.70$, and $\theta=0^{\circ}$.
 - (b) Tall deflectors; nominal NPR = 4.0.

Figure 10. Concluded.

- (a) Nominal NPR = 4.0.
- Figure 11. Effect of deflector height on nozzle internal performance characteristics with $A_e/A_t = 1.8$, $\delta_{v,p} = 0^{\circ}$, $X_s/L_f = 0.70$, and $\theta = 0^{\circ}$.
 - (b) Nominal NPR = 6.0.

Figure 11. Concluded.

- (a) Nominal NPR = 4.0.
- Figure 12. Effect of expansion ratio on nozzle internal performance characteristics with $\delta_{v,p} = 0^{\circ}$, $X_s/L_f = 0.70$, $\theta = 0^{\circ}$, and tall deflectors.
 - (b) Nominal NPR = 6.0.

Figure 12. Concluded.

(a)
$$\delta_{\text{defl}} = 0^{\circ}$$
.

Figure 13. Effect of sidewall modifications on nozzle internal performance characteristics with $A_e/A_t = 1.8$, $\delta_{v,p} = 0^{\circ}$, and tall deflectors.

(b)
$$\delta_{\text{defl}} = 30^{\circ}$$
.

Figure 13. Continued.

(c)
$$\delta_{\text{defl}} = 60^{\circ}$$
.

Figure 13. Continued.

(d)
$$\delta_{\text{defl}} = 90^{\circ}$$
.

Figure 13. Concluded.

Figure 14. Effect of nozzle pressure ratio on internal static pressure distributions with $A_e/A_t=1.8$, $\delta_{v,p}=0^\circ$, $X_s/L_f=0.70$, $\theta=25^\circ$, and $\delta_{\text{defl}}=0^\circ$.

(a)
$$\delta_{\text{defl}} = 0^{\circ}$$
.

Figure 15. Effect of sidewall modifications on internal static pressure distributions with $A_e/A_t = 1.8$, $\delta_{v,p} = 0^{\circ}$, and tall deflectors at nominal NPR of 4.0.

(b)
$$\delta_{\text{defl}} = 30^{\circ}$$
.

Figure 15. Continued.

(c)
$$\delta_{\text{defl}} = 60^{\circ}$$
.

Figure 15. Continued.

(d)
$$\delta_{\text{defl}} = 90^{\circ}$$
.

Figure 15. Concluded.

Figure 16. Effect of pitch vectoring on nozzle internal performance characteristics with $A_e/A_t = 1.8$, $X_s/L_f = 0.70$, $\theta = 0^{\circ}$, and $\delta_{\text{defl}} = 0^{\circ}$.

(a) Nominal NPR = 4.0.

Figure 17. Effect of pitch vectoring on internal static pressure distributions with $A_e/A_t = 1.8$, $X_s/L_f = 0.70$, $\theta = 0^{\circ}$, and $\delta_{\text{defl}} = 0^{\circ}$.

(b) Nominal NPR = 6.0.

Figure 17. Continued.

(c) Nominal NPR = 10.0.

Figure 17. Concluded.

- Figure 18. Effect of pitch vectoring on yaw-vectoring performance with $A_e/A_t=1.8,~X_s/L_f=0.70,$ short deflectors, $\delta_{\text{defl}}=45^{\circ},$ and $\theta=0^{\circ}.$
- Figure 19. Effect of yaw vectoring on pitch-vectoring performance with $A_e/A_t=1.8$, $\delta_{v,p}=20^{\circ}$, $X_s/L_f=0.70$, and short deflectors.

REPORT DOCUMENTATION PAGE				Form Approved OMB No. 0704-0188		
Public reporting burden for this collection of info gathering and maintaining the data needed, and collection of information, including suggestions in Davis Highway, Suite 1204, Arlington, VA 2220	ormation is estimated to average 1 hour per i completing and reviewing the collection of i for reducing this burden, to Washington Hea 2-4302, and to the Office of Management ai	response, including the time for nformation. Send comments reg dquarters Services, Directorate f nd Budget, Paperwork Reductio	reviewing instr arding this bur or Information n Project (070	uctions, searching existing data sources, rden estimate or any other aspect of this Operations and Reports, 1215 Jefferson 4-0188), Washington, DC 20503.		
1. AGENCY USE ONLY (Leave blank) 2. REPORT DATE September 1993 Technical Paper			D DATES C	COVERED		
4. TITLE AND SUBTITLE Effects of Internal Yaw-Vect Performance of a Pitch-Vect Convergent-Divergent Nozz 6. AUTHOR(S) Scott C. Asbury	toring Nonaxisymmetric			IG NUMBERS 05-68-70-06		
7. PERFORMING ORGANIZATION P NASA Langley Research Ce Hampton, VA 23681-0001				RMING ORGANIZATION T NUMBER 29		
9. SPONSORING/MONITORING AGENCY NAME(S) AND ADDRESS(ES) National Aeronautics and Space Administration Washington, DC 20546-0001			AGENO	SORING/MONITORING CY REPORT NUMBER A TP-3369		
11. SUPPLEMENTARY NOTES						
12a. DISTRIBUTION/AVAILABILITY	/ STATEMENT		12b. DISTI	RIBUTION CODE		
Unclassified-Unlimited Subject Category 02						
An investigation was conducted in the static test facility of the Langley 16-Foot Transonic Tunnel to evaluate the internal performance of a nonaxisymmetric convergent-divergent nozzle designed to have simultaneous pitch and yaw thrust-vectoring capability. This concept utilized divergent flap deflection for thrust vectoring in the pitch plane and flow-turning deflectors installed within the divergent flaps for yaw thrust vectoring. Modifications consisting of reducing the sidewall length and deflecting the sidewall outboard were investigated as means to increase yaw-vectoring performance. This investigation studied the effects of multiaxis (pitch and yaw) thrust vectoring on nozzle internal performance characteristics. All tests were conducted with no external flow, and nozzle pressure ratio was varied from 2.0 to approximately 13.0. The results indicate that this nozzle concept can successfully generate multiaxis thrust vectoring. Deflection of the divergent flaps produced resultant pitch vector angles that, although dependent on nozzle pressure ratio, were nearly equal to the geometric pitch vector angle. Losses in resultant thrust due to pitch vectoring were small or negligible. The yaw deflectors produced resultant yaw vector angles up to 21° that were controllable by varying yaw deflector rotation. However, yaw deflector rotation resulted in significant losses in thrust ratios and, in some cases, nozzle discharge coefficient. Either of the sidewall modifications generally reduced these losses and increased maximum resultant yaw vector angle. During multiaxis (simultaneous pitch and yaw) thrust vectoring, little or no cross coupling between the thrust-vectoring processes was observed.						
14. SUBJECT TERMS Multiaxis thrust vectoring; Multifunction nozzles; Nonaxisymmetric nozzle Nozzles; Thrust vectoring			s; 108 16. PRICE CODE			

18. SECURITY CLASSIFICATION 19. SECURITY CLASSIFICATION 20. LIMITATION

OF ABSTRACT

Unclassified NSN 7540-01-280-5500

OF REPORT

17. SECURITY CLASSIFICATION

OF THIS PAGE

 ${\bf Unclassified}$

Standard Form 298(Rev. 2-89) Prescribed by ANSI Std. Z39-18 298-102

OF ABSTRACT